View metadata, citation and similar papers at core.ac.uk

brought to you by CORE

provided by Newcastle University E-Prints

Arauzo A, Bartolomé E, Benniston AC, Melnic S, Shova S, Luzón J, Alonso PJ, Barra AL, Bartolomé J.

Slow Magnetic Relaxation in a dimeric Mn_2Ca_2complex enabled by the large Mn(III) rhombicity.

***Dalton Transactions,* 2016**

Copyright:

This is the authors accepted manuscript of an article that has been published in its final definitive form by Royal Society of Chemistry, 2016

DOI link to article:

http://dx.doi.org/10.1039/C6DT02509A

Date deposited:

09/12/2016

Embargo release date:

07 December 2017

This work is licensed under a Creative Commons Attribution-NonCommercial 3.0 Unported License

Newcastle University ePrints - eprint.ncl.ac.uk

Slow Magnetic Relaxation in a dimeric Mn_2Ca_2 complex enabled by the large Mn(III) rhombicity

Received 00th January 20xx,
Accepted 00th January 20xx

Ana Arauzo,[a] Elena Bartolomé,[b] Andrew C. Benniston,[c*] Silvia Melnic,[d] Sergiu Shova,[e] Javier Luzón,[f,g] Pablo J. Alonso,[g] Anne-Laure Barra[h] and Juan Bartolomé[g*]

In this paper we present the characterization of the complex with formula $[Mn_2Ca_2(hmp)_6(H_2O)_4(CH_3CN)_2](ClO_4)_4$ **(1)**, where hmp-H = 2-(hydroxymethyl)pyridine. Compound **1** crystallizes in the monoclinic space group C2/c with the cation lying on an inversion centre. Static magnetic susceptibility, magnetization and heat capacity measurements reflect a unique Mn(III) valence state, and single-ion ligand field parameters with remarkable large rhombic distorsion (D/k_B = -6.4 K, E/k_B = -2.1 K), in good agreement with. high-field electron paramagnetic resonance experiments. At low temperature the Mn_2Ca_2 cluster behaves as a system of ferromagnetically coupled (J/k_B= 1.1 K) Mn dimers with a S_T = 4 ground state. Frequency dependent ac susceptibility measurements reveal the slow magnetic relaxation characteristic of a Single Molecule Magnet (SMM) below T = 4 K. At zero magnetic field, an Orbach-type spin relaxation process ($\tau \sim 10^{-5}$ s) with an activation energy E_a = 5.6 K is observed, enabled by the large E/D rhombicity of the Mn(III) ions. Upon the application of a magnetic field, a second, very slow process ($\tau \sim 0.2$ s) is observed, attributed to a direct relaxation mechanism with enhanced relaxation time owing to the phonon bottleneck effect.

1. Introduction

Manganese complexes have been intensively investigated for many years, motivated first by the research of biologically important molecules (such as those involved in photosynthesis), [1] and more recently, the study of Single-Molecule Magnets (SMMs)[2] and Single-Chain Magnets (SCMs).[3] The important role played by manganese in photosynthesis cannot be overstated. In natural photosynthesis, solar energy is converted into chemical energy by utilizing water, which is catalytically converted to O_2 in the oxygen-evolving complex (OEC) of Photosystem II (PSII),[4] embedded in the thylakoid membranes of green plants, cyanobacteria and algae.[5,6] In particular, the Mn_3CaO_4 cubane cluster seems to be at the core of its functionality as OEC. The metal oxidation assignment in the oxygen evolving center established the presence of multiple manganese oxidation states (+3, +4).[7]

Besides, following the discovery in the 90's of slow relaxation in $[Mn(III)_4Mn(IV)_8O_{12}(O_2CMe)_{16}(H_2O)_4]$,[8] Mn-based SMMs have been exhaustively studied, with spin values ranging from S = 2[9] to S = 83/2[10] and nuclearities ranging from 1[11] to 84.[12] Mn(III) based complexes are of particular interest because of the large spin S = 2, and anisotropy arising from the ion's Jahn-Teller distorted octahedral coordination site. Additionally, di-nuclear $Mn(III)_2$ complexes are ideal to investigate the dependence of the magnetic properties on inter-ion coupling by different ligands. Thus, a plethora of $Mn(III)_2$ complexes have been studied, especially phenolic oxime-bridged complexes[13] and Mn(III)-Schiff base out-of-plane dimers.[14,15,16] Moreover, numerous manganese systems have been synthesized as models for the OEC.[1,17] In particular, tens of dinuclear Mn(III) complexes (Mn-μ-O-Mn, Mn-μ-O_2-Mn, Mn-μ-O_2-μ-O_2-Mn, imidazolate bridged…) have been reported and magnetically characterized.[1,18]

Some of the dimeric complexes have been characterized by dc magnetometry, and both ferromagnetic and antiferromagnetic interactions between the Mn…Mn ions have been reported.[19] However, slow relaxation of the magnetization in dimeric $Mn(III)_2$ complexes has been demonstrated in a few cases only, mostly under the application of a magnetic field, see Table 1.

[a] *Servicio de Medidas Físicas, Universidad de Zaragoza, Pedro Cerbuna 12, 50009 Zaragoza, Spain.*
[b] *Escola Universitària Salesiana de Sarrià (EUSS), Passeig Sant Joan Bosco 74, 08017 Barcelona, Spain.*
[c] *Molecular Photonics Laboratory, School of Chemistry, Newcastle University, Newcastle-upon-Tyne, NE1 7RU, UK.*
[d] *Institute of Chemistry, Academy of Sciences of Moldova, Academiei street 3, MD-2028, Chisinau, Moldova.*
[e] *Institute of Macromolecular Chemistry "Petru Poni" Iasi, Aleea Grigore Ghica Voda, nr. 41A, 700487 Iasi, Romania.*
[f] *Centro Universitario de la Defensa. Academia General Militar, Zaragoza, Spain.*
[g] *Instituto de Ciencia de Materiales de Aragón and Departamento de Física de la Materia Condensada, CSIC-Universidad de Zaragoza, Pedro Cerbuna 12, 50009 Zaragoza, Spain.*
[h] *Laboratoire National des Champs Magnetiques Intenses. CNRS, 25 rue des Martyrs, B.P. 166, 38042 Grenoble Cedex 9, France.*

Electronic Supplementary Information (ESI) available: SI1. Crystallographic data for complex **1**; SI2. Magpack simulations; SI3. HF-EPR measurements.

Table 1. Summary of magnetic parameters of reported Mn^{III}_2 SMMs.

Author	Ref	Complex	*g*	*J*(K)	*D*(K)	*E*(K)	z*J'*	U_{eff}(K),*H*	τ_0(s)
Miyasaka 2004	20	$[Mn_2(saltmen)_2(ReO_4)_2]$	2.00	2.65	-4.0	-	-	16 (0 Oe)	$8x10^{-9}$
Rajaraman 2005	21	$[Mn_2(Hthme)_2](ClO_4)_2$	1.71	3.05	-0.93	-	-	n.a.*	n.a.*
Lu 2006	14	$[Mn(saltmen)(O_2CCH_3)]_2.2CH_3CO_2H$ **(1)**	1.98	1.94	-1.4	-	-	27.8 (5.0 kOe)	$5.1\ x10^{-8}$
		$[Mn(saltmen)(N_3)]_2$ **(2)**		0.86	-1.4	-	-	17.0 (0 Oe) 28.7 (1kOe)	$6.8\ x10^{-8}$ $1.0\ x10^{-8}$
		$[Mn(salen)(NCO)]_2$ **(3)**		1.05	-0.43	-	-	23.5 (1.0 kOe)	$2.3\ x10^{-8}$
		[Mn(3,5-Brsalen) (3,5-Brsalicylaldehyde)]$_2$ **(4)**		0.79	-5.89	-	-	22.5 (1.0 kOe)	$4.6\ x10^{-8}$
Bhargavi 2009	15	$[Mn(salpn)NCO]_2$ **(1)**	2.02	0.60	$8.6\ x10^{-4}$	-	-	n.a.*	n.a.*
		$[Mn(salmen)N_3]_2$ **(2)**	2.00	0.77	-3.1			n.a.*	n.a.*
Wu 2009	16	$[Mn(salen)(H_2O)]_2Na[AlMo_6(OH)_6O_{18}].20H_2O$ **(1)**	1.98	0.89	~-4	-	-0.03	13.2 (0.7 kOe)	$7.2x10^{-7}$
		$[Mn(salen)(H_2O)]_2Cr[AlMo_6(OH)_6O_{18}].20H_2O$ **(2)**	1.92	0.63	~-4	-	-0.04	9.1 (0.6 kOe)	$1.6x10^{-6}$
Sawada 2012	22	$[Mn_2(5\text{-}MeOsaltmen)_2(acetone)_2]$-$[SW_{12}O_{40}]$ **(1)**	2.07	1.33	-4.17	-	0.016	15.9 (0.3kOe) 18.4 (0.6 kOe) 19.7 (1 kOe) 22.8 (1.5 kOe)	$6.1x10^{-7}$ $3.7x10^{-7}$ $3.2x10^{-7}$ $8.2x10^{-8}$
		$[Mn_2(salen)_2(H_2O)_2]_2[SiW_{12}O_{40}]$ **(2)**	2.09	0.98	-4.8		-0.856	15.4(1.0 kOe) 21.2 (1.5 kOe)	$4.1x10^{-7}$ $4.4x10^{-8}$
		$[Mn(5\text{-}BrSaltmen)(H_2O)(acetone)]_2$ $[\{Mn_2(5\text{-}BrSaltmen)_2\}(SiW_{12}O_{40})]$ **(3)**						14.7 (0.5kOe) 17.6 (1.0 kOe) 21.0 (1.5 kOe)	$3.8x10^{-7}$ $2.4x10^{-7}$ $6.4x10^{-8}$
		$[Mn(salmen)N_3]_2$ **(2)**	2.00	0.83	-3.34	-	-	n.a.*	n.a.*
Bhargavi 2013	23	$[Mn(5\text{-}Clsalpn)N_3]_2$	2.02	1.00	-1.44	-	0.036	18.2 (0 Oe) 26 (3 kOe)	$5.77x10^{-8}$ $4.05x10^{-8}$
Wang 2014	24	$[Mn_2(5\text{-}Brsalen)_2\ (C_{10}H_7PO_3H)_2]\cdot 2CH_3OH$ **(1)**	1.97	1.33	~-2	-	-0.06	21.8 (2kOe)	$7.1x10^{-8}$
This work		$[Mn_2Ca_2(hmp)_6(H_2O)_4(CH_3CN)_2](ClO_4)_4$	2.06	1.1	-6.4	-2.1	-	5.6 (0 Oe) 5.6 (2.5 kOe)	$2.2\ x\ 10^{-6}$ $2.2\ x\ 10^{-6}$

n.a.* (not applicable). Observed relaxation, no data.

The inclusión of Ca as a structure-stabilizing atom in the cluster has attracted much attention. Recently, the magnetic properties of mixed Mn/Ca metal clusters have been studied in a few cases. The first detailed magnetic investigation of such compounds was reported for $[CaMn(III)_3Mn(II)(\mu_4O)(L)_3Cl_2(O_2CMe)_{1.2}(H_2O)_{1.5}(MeOH)_{0.3}]Cl_{0.8}\cdot 5MeOH$ in 2006,[25,26] and in 2010, for the mixed metal cluster $\{[Mn(III)_3NaCa(sal)_6(H_2O)_6]\cdot 7H_2O\}_n$.[27] Several other complexes have been reported, including $(NHEt_3)_2[Mn(III)_4Ca(O_2CPh)_4(shi)_4]\cdot 4CH_2Cl_2$[28] and $[\{Mn(III)_6Ca_2O_2(Me\text{-}saO)_6(prop)_6(H_2O)_2]\cdot 2MeCN\cdot 0.95H_2O\}_n$.[29] In 2013, the magnetic properties of two complexes incorporating a $Mn(IV)_3CaO_4$ core (with a high degree of structural similarity to the OEC) were investigated by Krewald *et al.*[30] All these works demonstrated that various mixed Mn/Ca compounds could be prepared, their analysis being crucial for the understanding of the function and properties of the Kok states for the OEC. There is growing evidence showing that Ca provides a structural framework which helps manganese access higher oxidation states at a lower potential. Therefore, it is essential the study of Mn/Ca heteronuclear complexes which mimic the structure of PSII in order to investigate the structural effects of calcium in Mn(III) ions, and how its electronic structure is therefore affected.

It is worth mentioning that, so far, the magnetic relaxation behaviour of polynuclear Mn/Ca complexes has been seldom investigated. In 2014, our group reported the first example of a field-induced SIM based on a Mn(II)/Ca complex.[31]

In this paper we present the synthesis, structure, *ab inito* calculations, thermo-magnetic and high-field electron paramagnetic resonance (HF-EPR) characterization of a rare example of a noncarboxylate Mn(III)/Ca complex, $[Mn_2Ca_2(hmp)_6(H_2O)_4(CH_3CN)_2](ClO_4)_4$, **1**, showing SMM behaviour, even in a zero applied magnetic field. For our new compound we used 2-(hydroxymethyl)pyridine (hmp-H) that belongs to the family of pyridine based alkoxide compounds and it is known to be an excellent bridging and chelating ligand. Commonly hmp-H ligand chemistry is dominated by homo- and

heteropolynuclear 3d,[32] 3d/3d[33] as well as 3d/4f [34,35] metal clusters. It was found that it can support ferromagnetic coupling between these metal atoms yielding interesting series of compounds with large S values and SMM behavior. Even though numerous complexes have been synthesized with hmp-H, it has not been employed to date in mixed Mn/Ca compounds.

2. Materials and Experimental Methods

2.1 Experimental Techniques

The dc magnetization and ac susceptibility of powdered samples were measured, from 1.8 K to 300 K, using a Quantum Design superconducting quantum interference device (SQUID) magnetometer. Ac measurements were done at fixed temperatures in the range $1.8 < T < 10$ K, with an excitation field of 4 Oe, at dc bias fields in the range $0 < H < 50$ kOe, while sweeping the frequency $0.1 < f < 10000$ Hz. Low frequency range (0.1 Hz – 1 kHz) was measured with SQUID magnetometer and high frequency range (10 Hz – 10 kHz) in a Quantum Design PPMS ACMS magnetometer. Measurements on powdered samples were performed with the addition of Daphne oil, introduced to fix the grains at low temperatures.

Heat capacity $C(T)$ was measured as a function of temperature under different applied fields (0 - 30 kOe) using the same PPMS, equipped with a ^{3}He refrigerator. Samples were prepared as pressed powder pellets and fixed to the sampleholder with Apiezon N grease.

HF-EPR spectra were recorded on a laboratory-made spectrometer using powder samples pressed in pellets to avoid preferential orientation of the crystallites in a strong magnetic field. The radiation source used is a Gunn diode operating at 110.4 GHz and equipped with a harmonics generator to record spectra at 110.4, 220.8, 331.2 and 441.6 GHz.[36] The experiment was performed at 5, 15 and 30 K, and the field was produced by a superconducting magnet (0 – 160 kOe).

Crystallographic measurements for $[Mn_2Ca_2(hmp)_6(H_2O)_4(MeCN)_2](ClO_4)_4$ **1** were performed on an Oxford-Diffraction XCALIBUR E CCD diffractometer equipped with graphite-monochromated Mo-Kα radiation. The single crystal was positioned at 40 mm from the detector and 222 frames were measured each for 8 and 10 s over 1° scan width. The unit cell determination and data integration were carried out using the Oxford Diffraction CrysAlis package.[37] The structure was solved by direct methods using Olex2[38] software with the SHELXS structure solution program and refined by full-matrix least-squares on F^2 with SHELXL-97.[39] CCDC-1482905 contains the supplementary crystallographic data for this contribution, which can be obtained, free of charge via www.ccdc.cam.ac.uk/conts/retrieving.html (or from the Cambridge Crystallographic Data Centre, 12 Union Road, Cambridge CB2 1EZ, UK; fax: (+44) 1223-336-033; or deposit@ccdc.ca.ac.uk). Data pertaining to the crystal structure of **1** are collected in SI1.

2.2 Materials

All chemicals were purchased from commercial sources and used as received without further purification. The solid N-n-Bu_4MnO_4 was prepared according to the literature.[40] All manipulations were performed under aerobic conditions.

Preparation of $[Mn_2Ca_2(hmp)_6(H_2O)_4(MeCN)_2](ClO_4)_4$ (1)
The precursor $[Mn_3O(\alpha\text{-fur})_6(py)_2H_2O]$ (0.1 g, 0.097 mmol), $Ca(ClO_4)_2{\cdot}4H_2O$ (0.2 g, 0.6 mmol) and 2-(hydroxymethyl)pyridine (hmp-H) (0.11 g, 1 mmol) were dissolved in MeCN. The resulting solution was stirred overnight at room temperature. The dark pink solution was filtered and was kept sealed for three days to give well-formed pink crystals, which are soluble in methanol and DMF. Elemental analysis calc. for $C_{44}H_{56}Ca_2Cl_4Mn_2N_{10}O_{26}$: C, 35.88%; H, 3.83%; N, 9.51%. Fnd: C. 35.69%; H, 3.76%; N, 9.33%. I.R. (cm^{-1}): 3507, 1606, 1486, 1440, 1372, 1280, 1039b, 931, 823, 762, 724, 622.

Preparation of precursor $[Mn_3O(\alpha\text{-fur})_6(py)_2H_2O]$ (2)
The synthesis was carried out by adapting a literature procedure.[41] $Mn(CH_3COO)_2{\cdot}4H_2O$ (0.2 g, 0.81 mmol) and α-furancarboxylic acid (α-fur-H) (0.68 g, 6.07 mmol) were dissolved in pyridine (0.3 mL) and ethanol (10 mL). Solid N-n-Bu_4MnO_4 (0.11 g) was added in small portions with stirring to give a brown homogeneous solution. After 24 h, the resulting grey precipitate was filtered off, washed with ethanol and dried. Recrystallization was accomplished by allowing a MeCN/THF solution to slowly concentrate by evaporation to give black crystals, which were collected by filtration, washed and dried. Elemental analysis calc. for $C_{40}H_{30}Mn_3N_2O_{20}$: C, 46.94%; H, 2.95%; N, 2.74%. Fnd: C. 46.72%; H, 2.76%; N, 2.63%. I.R. (cm^{-1}): 3123, 1615, 1576, 1475, 1409, 1370, 1224, 1195, 1142, 1073, 1045, 1012, 933, 883, 780, 757, 688, 614.

3. Results and Discussion

3.1 Synthesis

Complex $[Mn_2Ca_2(hmp)_6(H_2O)_4(CH_3CN)_2](ClO_4)_4$ **1** represents a rare example of a carboxylate-free mixed-metal cluster. The complex was synthesized in two steps starting from the precursor $[Mn_3O(\alpha\text{-fur})_6(py)_2H_2O]$ **2**, where α-fur is an α -furancarboxylic acid. The design idea was to use the excellent N,O bridging and chelating ligand 2-(hydroxymethyl)pyridine (hmp-H) and the μ_3-O tri-manganese furan carboxylate complex to form a mixed ligand manganese-calcium cluster. Thus, mixing of $[Mn_3O(\alpha\text{-fur})_6(py)_2H_2O]$ **2** with $Ca(ClO_4)_2{\cdot}4H_2O$ in MeCN at room temperature, followed by leaving the solution overnight, resulted in a dark pink solution. Upon standing for several days a pink crystalline material was isolated from the solution in a good yield (~80%). Under the synthesis conditions the furoate ligands are essentially "lost" and the chelation properties of the hmp-H ligands dominate. The FT-IR spectrum of the sample was consistent with the presence of some general characteristic bands. A broad absorption band at 3507 cm^{-1} appears due to the stretching frequency ν(O–H) of the coordinated H_2O. A typical CO stretching mode for an alkoxy residue was observed at 1039 cm^{-1}. Additional features in the FT-IR spectrum for **1** included a series of absorption bands in the 1606–1440 cm^{-1} region that were attributed to the pyridyl groups {ν(C=C) and ν(C=N)}.

Table 2. Selected bond lengths (Å) and angles (°) for structure **1**.

Mn-O1	1.975(3)	Ca-O2[1]	2.332(3)
Mn-O1[1]	2.289(3)	Ca-O3	2.347(3)
Mn-O2	1.869(3)	Ca-O1*w*	2.356(4)
Mn-O3	1.865(3)	Ca-O2*w*	2.347(4)
Mn-N2	2.202(4)	Ca-N1	2.516(4)
Mn-N3	2.061(4)	Ca-N4	2.543(6)
		Ca-O1	2.460(3)
O1-Mn-O1[1]	79.2(1)	O3-Mn-O1	86.2(1)
O1-Mn-N2	98.2(1)	O3-Mn-O2	175.6(2)
O1-Mn-N3	165.0(2)	O3-Mn-N2	98.2(2)
O2-Mn-O1[1]	82.8(1)	O3-Mn-N3	81.9(2)
O2-Mn-O1	98.0(1)	N2-Mn-O1[1]	161.9(1)
O2-Mn-N2	79.8(2)	N3-Mn-O1[1]	93.9(1)
O2-Mn-N3	94.3(2)	N3-Mn-N2	92.4(2)
O3-Mn-O1[1]	99.6(1)	O1-Ca-N1	66.6(1)
O1-Ca-N4	131.4(2)	O2W-Ca-O1	124.0(2)
O1W-Ca-O1	136.2(1)	O2W-Ca-O1*w*	83.2(2)
O1W-Ca-N1	157.0(2)	O2W-Ca-N1	83.5(2)
O1W-Ca-N4	79.3(2)	O2W-Ca-N4	84.5(2)
O2[1]-Ca-O1	70.5(1)	O3-Ca-O1	66.1(1)
O2[1]-Ca-O1*w*	84.7(1)	O3-Ca-O1*w*	80.9(1)
O2[1]-Ca-O2Iw	165.5(2)	O3-Ca-O2*w*	92.0(1)
O2[1]-Ca-O3	94.0(1)	O3-Ca-N1	118.3(1)
O2[1]-Ca-N1	105.1(1)	O3-Ca-N4	160.1(2)
O21-Ca-N4	85.4(2)	N1-Ca-N4	80.8(2)

Symmetry code: [1)] 0.5 - *x*, 1.5 - *y*, 1 – *z*

Elemental analysis of the complex was consistent with its molecular formula.

3.2. Crystal Structure

The title complex **1** crystallizes in the monoclinic space group C2/c, and the molecular structure is shown in Figure 1. A collection of selected bond lengths and angles is given in Table 2. The calcium(II) ion is 7-coordinated (distorted pentagonal bipyramid) and the coordination sphere comprises a N_2O_5 donor set. Ligation to the calcium ion is provided by two water molecules, an acetonitrile, two μ_2-O atoms from hmp ligands and a μ_3-O from a single hmp. The Jahn-Teller-like distorted octahedral manganese(III) ion is made up of a N_2O_4 donor group, with two μ_3-O, two μ_2-O and two N atoms completing the coordination sphere. Hmp ligand manifests as bridging as well as chelating agent. A simplified Mn_2Ca_2 motif core is observed for structure **1** by just considering the donor atoms (Figure 1, top right). Interestingly, the only similar type of structure was reported by Jerzykiewicz *et al.*,[42] but for a Mn_4Ca_2 core. The Mn-Mn and Ca-Ca separation distances within the Mn_2Ca_2 core are 3.2906(9) Å and 6.070(2) Å, respectively. The Ca-Mn distances (Table 2) are similar to those found in the natural cubane structure for the OEC. The adjacent pyridine rings of hmp ligands are not within range to form a π-stack, and are divergent by 24.5° using planes created from each separate ring (Figure 1, bottom left). The cuboid-like arrangement reveals slightly different Ca-O bond lengths for the bridging Ca-O-Mn units. Because of the Jahn-Teller-like distorted octahedral geometry at the Mn(III) ion, bond lengths are very dissimilar. The distorted octahedral quasiaxes follow the length trend O1-Mn-N2 > N3-Mn-O1 > O3-Mn-O2 (Figure 2). Notably, the coordination environment around each Mn shows a remarkably large rhombic distortion, as the bond lengths and angles evidence a highly distorted octahedron far from ideal D_{4h} symmetry.

The crystal packing diagram (Figure 3) shows the projection down the c-axis, highlighting the solvate acetonitrile molecules in the structure channels. Certainly interesting is the lack of solvate molecules in all the cavities, so that only each alternate channel is filled. The nitrogen atom of the acetonitrile is hydrogen bonded to a water molecule from the calcium ion.

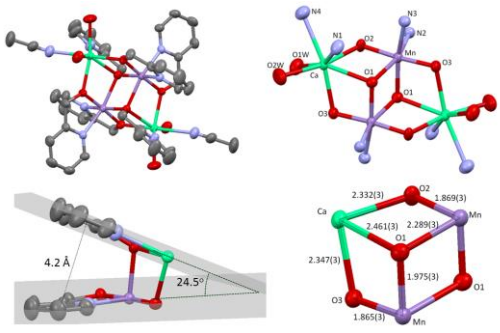

Figure 1. Top: Molecular structure for complex **1** shown as 50% ellipsoids (left) and the basic coordination chemistry with labels at the manganese and calcium ions (right). Bottom: Representation of two adjacent pyridine groups and the distance and angle between the rings (left), and the basic cuboid-like arrangement and bond lengths (in Å) (right). Hydrogens are omitted for clarity along with solvent molecules and counter ions.

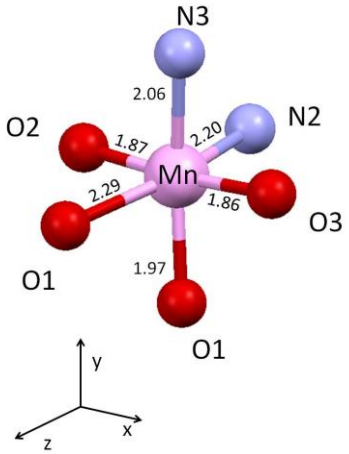

Figure 2. Detail of the Mn(III) coordination environment and bond lengths (in Å) to the N2O4 donor group, evidencing the highly distorted octahedral geometry.

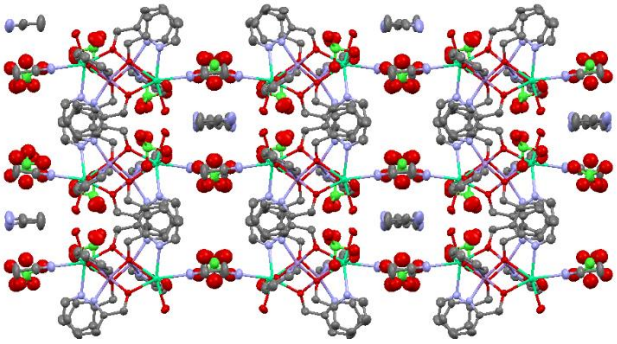

Figure 3. Crystal packing diagram for **1** viewed down the *c*-axis. Hydrogens are omitted for clarity. Solvent acetonitrile molecules and the positioning of the disorded perchlorate anions are shown in the channels.

3.3. *Ab initio* calculations

Ab initio calculations were performed using the CASSCF/NEVPT2 method,[43] as implemented in the ORCA quantum chemistry package.[44] In this method the spin–orbit coupling and the spin–spin coupling relativistic effects, which are at the origin of the magnetic anisotropy, are included *a posteriori*. The *ab initio* calculations were done on a quantum cluster of atoms obtained from the experimental structure. The quantum cluster consisted of a $Mn_2Ca_2(hmp)_6(H_2O)_4$ molecule in which one of the Mn(III) ions was replaced by a diamagnetic Ga(II) ion. The basis-sets were the TZVP-DKH[45] for the Mn(III) ion, and for the first and second shells of atoms around it and the SVP-DKH[45] for all the other atoms.

In the CASSCF calculations the active space consisted of the Mn(III) 3d orbitals containing 4 electrons (CASSCF(4,5)). The state-averaged CASSCF calculation included 5 quintets and 35 triplets. Then, the NEVPT2 calculations were performed with the CASSCF(4,5) reference space for the treatment of the dynamical correlation energy. After that, the effect of the spin-orbit coupling was taken into account using a mean-field operator which is diagonalized in the basis of the previous CASSCF wavefunctions.

The following energy levels for the Mn(III) single-ion were obtained: 0.0, 1.13, 11.32, 19.48 and 21.26 K. Results show a rhombic geometry with ligand-field parameters D/k_B = -4.6 K and E/D = 0.29. The calculated Mn(III) easy axis of magnetization (EAM) lies approximately along the elongated O1-Mn-N2 coordination axis (Figure 4). The eigenfunctions corresponding to the energy eigenvalues given above, when described in the reference frame with the *z* direction defined by the easy magnetization axis, are $|2^s>$, $|2^a>$, $|1^s>$, $|1^a>$ and $|0'>$, respectively, as defined in reference [46]. As both Mn(III) ions are related by an inversion centre, they are crystallographically equivalent, having both the same EAM orientation and ligand field parameters.

In addition, in order to have a theoretical prediction of the ferro or antiferromagnetic nature of the magnetic super exchange interaction between the two Mn(III) ions, a Broken Symmetry DFT calculation[47] was also performed with the same ORCA quantum chemistry package.[44] The calculation was done using the B3LYP exchange-correlation functional[48] and the TZVP[45] basis-set for all atoms. No relativistic corrections were considered in this calculation The computed magnetic interaction was J/k_B = 0.22 K, of ferromagnetic nature. This result was expected since the two intervening Mn(III) wavefunctions are orthogonal and the Mn-O1-Mn angle is larger than 90º.

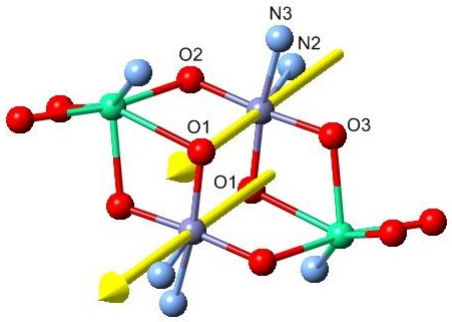

Figure 4. *Ab initio* calculated easy axes of magnetization of the two Mn(III) ions in the Mn_2Ca_2 dicubane-like core, in parallel, ferromagnetic configuration. The EAM of each ion points along the O1-Mn-N2 direction.

3.4 Static Magnetic Properties

The equilibrium dc magnetic susceptibility $\chi(T)$ of **1** was measured from 1.8 K to 300 K with a dc field of H = 1 kOe. In Figure 5 the $\chi T(T)$ curve is depicted. The room temperature value of $\chi T(T)$ is 6.4 emu.K/mol, which agrees well with the value predicted for two high-spin Mn(III) d^4 ions, each with the spin S = 2 and gyromagnetic factor g = 2.06 ± 0.05. As temperature is lowered the χT product increases, reaching a maximum at about T_{max} = 7 K. This behaviour is indicative of the presence of ferromagnetic coupling between the two Mn(III) ions, confirming the magnetic dimer. Below 7 K, the χT product decreases indicating the presence of inter-molecular antiferromagnetic interactions and/or zero-field splitting of the ground magnetic states. Given the crystal packing of the present compound and the distance in between molecules, we can neglect inter molecular magnetic interactions. Therefore the drop in the χT product can be ascribed to the thermal depopulation of Zero Field Splitted energy levels of the $Mn(III)_2$ ions.

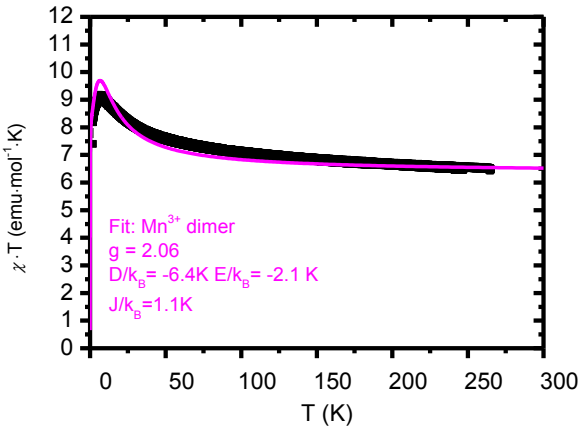

Figure 5. Temperature dependence of the product χT (at H = 1 kOe). In pink, simulation of the χT product for two Mn(III) ions (each with spin S = 2, ZFS parameters D/k_B = -6.4

K and E/k_B = -2.1 K, gyromagnetic value g = 2.06), with ferromagnetic coupling, J/k_B = 1.1 K.

The isothermal magnetization curves $M(H)$, measured at T = 1.8, 2.5, 3.5 and 5 K show a continuous increase for increasing field, without reaching saturation (Figure 6).

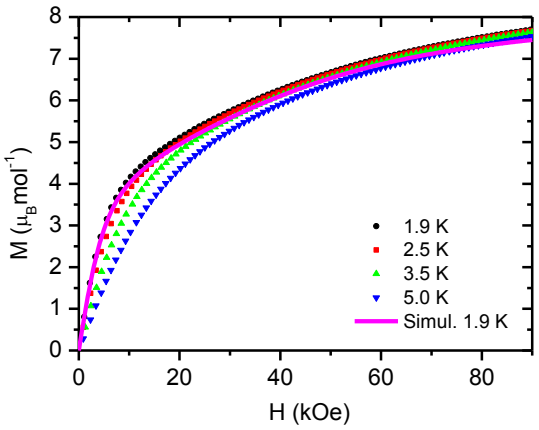

Figure 6. Magnetization in Bohr magnetons per Mn dimer as a function of magnetic field at T = 1.9, 2.5, 3.5 and 5 K. Simulated curve at T = 1.9 K for best fit parameters of Eq. [1] is shown in pink.

In addition, heat capacity measurements were performed as a function of temperature between 0.35 K and 160 K under different applied fields (Figure 7). The lattice contribution dominates $C(T)$ above 4 K, though there is a distinct bump at $T \approx 7$ K, which does not depend on the applied field. In contrast, the low temperature C increases for increasing field and shows a maximum within the temperature window of the experiment. This low temperature maximum shifts to higher temperature with increasing field. The lattice contribution was fitted to a potential function of temperature, $C_{lat} = A*T^n$ (A = 0.0669 R K^{-n} and n = 1.8) and removed from the total measured heat capacity to obtain the magnetic contribution per dimer, C_m (see Figure 8(a)). Note that the ratio $b = (C_m + C_{lat})/C_{lat}$ varies with temperature and applied field. While $b \approx 1$ at any field and $T \geq 3$ K, it increases for $T <$ 3K as the applied field increases. At T = 2 K and H = 5 kOe we estimate $b \approx 2$.

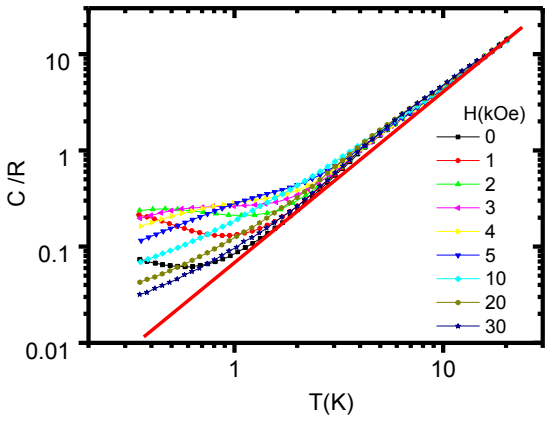

Figure 7. C(T) per Mn dimer for different applied magnetic fields. The lattice heat capacity is depicted by the thick red line.

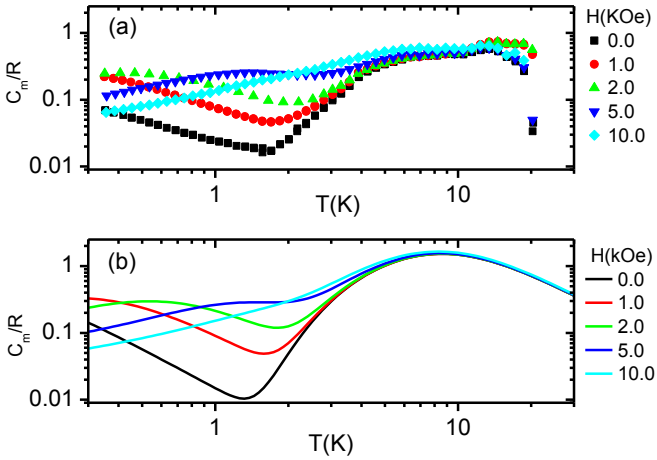

Figure 8. a) Magnetic heat capacity as a function of temperature for different applied fields. Lattice contribution has been removed. b) Simulated C_m/R values per dimer at different fields as obtained for dimer model given in Eq [1].

The magnetic properties of the complex can be described with the following effective multi-spin Hamiltonian:

$$H_{dim} = \sum_{i=1,2}\left[DS_i^{z,2} + E\left(S_i^{x,2} - S_i^{y,2}\right)\right] - 2J\left(\vec{S}_1 \cdot \vec{S}_2\right) + \sum_{i=1,2} g\mu_B \vec{S}_i \cdot \vec{H} \quad , \quad [1]$$

where the first term describes the Mn(III) single-ion ligand field (LF) anisotropy of orthorhombic symmetry (up to second order), caused by the {Mn(O^{hidrox})$_4$(N^{Py})$_2$} coordination. Since both Mn(III) are related crystallographically by an inversion centre, we assume that the ligand field constants are identical for both ions. This term is also defined as Zero-Field Splitting (ZFS). The second term corresponds to the intra-dimer exchange interaction, and the third term is the Zeeman term in an applied field.

Simulations of the static properties, $\chi T(T)$, $M(H)$ and $C_m(T)$ were performed under this model, implemented in MAGPACK.[49] The ZFS parameters (E, D), the exchange interaction (J) and gyromagnetic value were determined as the best set of parameters simultaneously fitting the $\chi T(T)$, $M(H)$ and C_m at H = 0 data (see ESI). The predictions were averaged over a random angle distribution. The value of the gyromagnetic value

(g = 2.06 ± 0.05) is essentially determined from the saturation of the χT at high temperature (300 K). The intra-dimer ferromagnetic constant affects mainly the position of the $\chi T(T)$ peak, from which it is obtained J/k_B = +1.1 ± 0.1 K. The $M(H)$ and $C_m(T, H = 0)$ curves could be fitted with the predictions obtained from Eq. [1] with the single-ion parameters D/k_B = -6.4 ± 0.2 K and E/k_B = -2.1 ± 0.2 K. Indeed, the high temperature contribution to the heat capacity, which is almost magnetic independent, is mainly due to the ZFS splitting parameter D, while the upturn at lower temperatures owes to the transversal parameter E.

As a check of the parameters, we verified using a home-made code that the $C_m(T)$ data at different applied fields could be well predicted by the heat capacity calculated using the Hamiltonian [1] (see Figure 8(b)).

At low temperatures, the intra-dimer ferromagnetic interaction gives a S_T = 4 ground state for the polynuclear Mn_2Ca_2 cluster. Figure 9a displays the energy levels calculated for the $Mn(III)_2$ dimer, according to the Hamiltonian [1], using the above determined exchange (J) and single-ion ZFS parameters (D, E). The dimer ground state is well described by the doublet $|S_T, \pm M_{S_T}\rangle = |4, \pm 4\rangle$, which displays a zero field splitting energy of Δ_{2Mn} = 0.25 K. This splitting is entirely due to the rhombic contribution (E) of the ZFS term of the Hamiltonian. The next excited levels, corresponding to the remaining states of the total spin $S_T = S_1 + S_2$ multiplet (25 levels $|S_T, \pm M_{S_T}\rangle$ for S_T = 4, 3, 2, 1 and 0) are well separated in energy by more than 15 K from the ground state. The thermal population of those levels gives rise to the rounded maximum observed at $T \approx 7$ K.

For the sake of comparison, the corresponding energy levels for the Mn(III) single-ion are displayed in Figure 9b. It is worth noting that the ground doublet energy splitting for the dimer, Δ_{2Mn} = 0.25 K, is considerable smaller than the splitting of Mn(III) single-ion $|2, \pm 2\rangle$ ground state doublet, $\Delta_{Mn} = 3E^2/D$ = 2.07 K.[50]

The C_m upturn of the dimer $Mn(III)_2$ at $T < 1$ K corresponds to the depopulation of the $|4, -4\rangle$ level and gives rise to a typical 2-level Schottky anomaly with a predicted maximum at T_{max} = 0.42*Δ_{2Mn} = 0.10 K. Therefore, the low temperature heat capacity measurement allows the experimental determination of the rhombic contribution to the ligand field of Mn(III) in this compound.

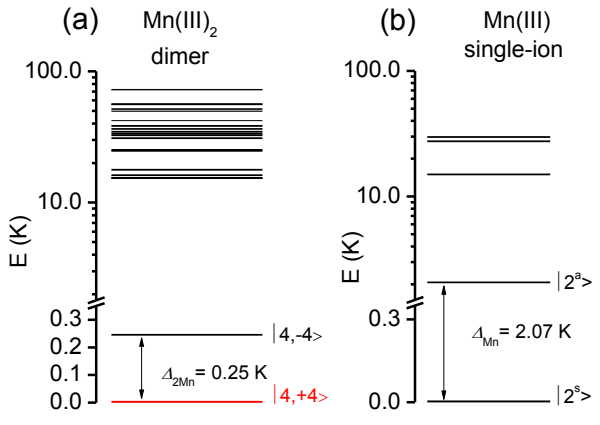

Figure 9. (a) Zero-field energy level diagram for the $Mn(III)_2$ dimer with J/k_B = 1.1 K, D/k_B = -6.4 K and E/k_B = -2.1 K, where the small splitting of the ground state, Δ_{2Mn} = 0.25 K, is observed; (b) the energy levels for a single Mn(III) ion are displayed for comparison; the ZFS of the ground state, Δ_{Mn}, is significantly larger.

Additional possible contributions to the zero field heat capacity at low temperature, namely, inter-dimer exchange and hyperfine interaction, have been discarded for the following reasons.

Certainly, in case the inter-dimer exchanges were causing the $T < 1$ K upturn, the $C_m(T)$ slope should be fitted with the T tail of an inter-dimer interaction contribution. This fit would give an exchange interaction of zJ'/k_B = 0.012 K (equivalent to a molecular field of H_m = 0.25 kOe). This value is much higher than what we could expect in this compound, where crystal packing of $[Mn_2Ca_2(hmp)_6(H_2O)_4(CH_3CN)_2]$ is achieved mainly by hydrogen bonds (see Figure 3). The adjacent pyridine rings of hmp ligands are not within range to form a π-stack, so indirect exchange can be neglected. Moreover, dipolar interaction contribution is also negligible at this level, given the separation of the molecules in the crystal structure.

On the other hand, hyperfine contribution as due to the interaction with ^{55}Mn nucleus, I = 5/2, μ = 3.4532 μ_N and 100% natural abundance, may appear at very low temperatures. The expected high temperature tail in that case would be:

$$C_{hf} = nN_A \frac{I(I+1)\mu^2 H_{hf}^2}{3k_B T^2} = \frac{A_{hf}}{T^2}\ , \qquad [2]$$

where n is the total number of nuclei having the nuclear spin quantum number I, μ_N is the nuclear Bohr magneton and H_{hf} is the average hyperfine field acting on the nuclear moment. The contribution has been calculated taking as a reference the nuclear magnetic resonance spectroscopy of $Mn_{12}Ac$,[51] which gives values for Mn(III) of up to 365 MHz, which is equivalent to H_{hf} = 138.7 kOe. The so obtained T^{-2} slope, is A_{hf}/R = 0.002 K^2, much smaller than the experimental low T heat capacity slope, so hyperfine contribution can be also dismissed.

In conclusion, heat capacity measurements confirm that the Mn_2Ca_2 cluster behaves as a Mn(III)-Mn(III) dimer with a zero-field splitting owing to the large transverse anisotropy of each ion in a low symmetry coordination environment, $\{Mn(O^{hidrox})_4(N^{Py})_2\}$.

The determined negative D value is consistent with an axial elongation which can be attributed to the O1-Mn-N2 axis in agreement with Mn(III) coordination (see Table 2) and *ab initio* calculations. The obtained D/k_B = -6.4 ± 0.2 K and E/D ~ 1/3 are in reasonable agreement with *ab initio* results, where also a remarkably large rhombicity, E/D = 0.29, is calculated. Furthermore, a noticeable rhombicity is expected in view of the large distortion of the crystallographic octahedron around Mn(III), see Figure 2. Note that the two N2 and N3 atoms belong to different quasi-axes of the distorted octahedron, thus adding to the rhombicity of the ligand field.

The obtained ZFS parameters are comparable to those found in literature for other Mn(III) ions in a distorted octahedral symmetry.[52,53,54] Axial $|D/k_B|$ values are in the range of 3 - 7 K,

being maximum for oxygen-based ligands. The rhombicity, however, is very sensitive to the coordination sphere, E/D ranging from 0 to 0.23.[52]

The intra-dimer exchange interaction is ferromagnetic, as predicted from *ab initio* calculations, though five times larger. Such magnitude difference is not surprising since DFT calculations have a semiquantitative precision in the determination of the magnetic coupling constants between transition-metals when the J value is of only a few Kelvin[55,56]. We may assume that at T = 0 K the magnetic moments (axial vectors related by the inversion center), are parallel one to each other as shown in Figure 4.

3.5 High-Field EPR spectroscopy

In order to confirm the orthorhombic character of Mn(III) magnetic anisotropy in this dimeric complex, high-field electron paramagnetic resonance (HF-EPR) measurements were conducted at different frequencies and temperatures.

The observed results at T = 5 K are depicted in Figure 10. In all the cases a signal at g ≈ 2 is observed. It consists of a narrow structureless line in 110.4 GHz and 220.8 GHz spectra. In both cases it is the only clear signal above the background line. The narrow line-shape suggests that it could be due to an undesired impurity. However in the 331.2 and 441.6 GHz spectra the g ≈ 2 signal shows a complex character: superimposed to the narrow spurious signal another broader one is observed, which decreases strongly when the temperatures increases. In fact it is barely seen in the 15 K spectra, and in the spectra taken at 30 K only the narrow line is detected (see Figure SI2). A similar feature is also observed in the 441.6 GHz spectra (not shown).

Besides, in the high frequency spectra some other lines can be clearly observed. In particular, in the 331.2 GHz spectrum prominent peaks are detected at a field lower than 10 kOe, suggesting a zero field splitting close to 15 K, in agreement with the energy level scheme given in Figure 9 for Mn(III). When a frequency of 441.6 GHz is used, a slightly asymmetric prominent signal at about 40 kOe is observed, together with some minor features at lower fields. In any case, the spectra are rather poor and, consequently a fitting process with the aim of obtaining an univocal determination of the spin-Hamiltonian parameters could not be undertaken.

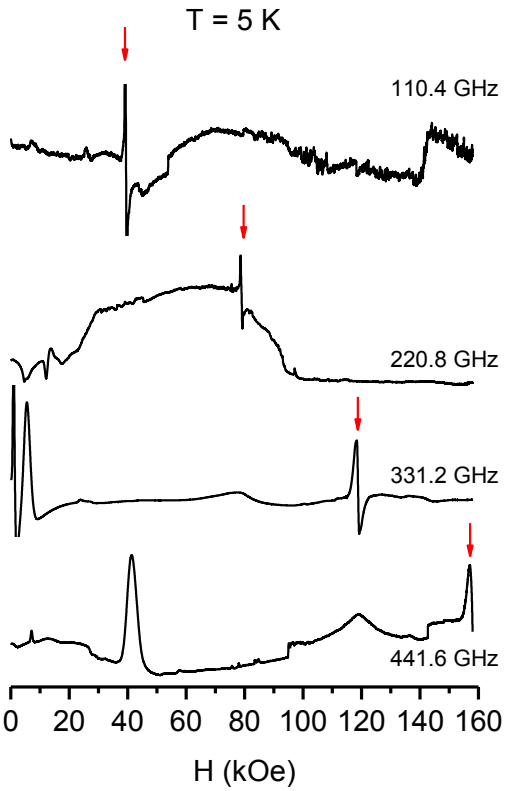

Figure 10. HF-EPR spectra of a powder Mn_2Ca_2 pellet, taken at T = 5 K, in arbitrary units. Red arrow indicates signal at g ≈ 2.

On the other hand, we have simulated the EPR spectra using the spin-Hamiltonian given by equation [1]. Simulations were performed with the Easyspin program.[57] The model proposed was a Mn(III)-Mn(III) dimer with identical reference axis system for both ions and coupled by ferromagnetic interaction. As starting parameters the single ion Mn(III) anisotropy parameters deduced from the low temperature thermomagnetic study were employed. The orthorhombicity ratio E/D was scanned in the parameter region $0 < E/D < 1/3$. The simulated spectra were compared to the experimental ones measured at 331.2 and 441.6 GHz, whose signal was sufficiently clear to support comparison.

Figure 11 shows the experimental spectra for 331.2 and 441.6 GHz (upper traces) together with the calculated ones (lower traces), using the parameters given above, D/k_B = -6.4 K, E/k_B = -2.1 K and a lorentzian line shape with a peak-to-peak width of 1 kOe. The main peak features of the spectra are predicted reasonably with the above parameters, admitting only slight variations of parameters of less than ten per cent.

Moreover, a strong variation of the orthorhombic ratio ($\eta = E/D$) results in drastic qualitative changes in the spectra, which are only compatible with a value of η around 1/3, as illustrated in Figure SI3.

We conclude that the HF-EPR experiment confirms the large orthorhombicity deduced from the combination of macroscopic measurements ($M(H)$, χ_{ac} and $C(T)$), and indicates that the orthorhombicity is close to the maximum one.

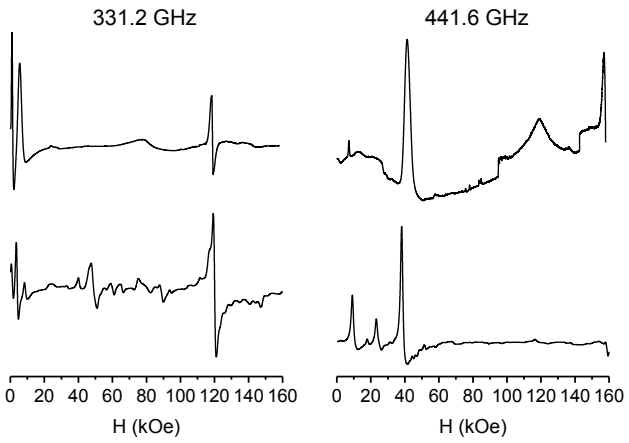

Figure 11. Comparison of the experimental spectra taken at T = 5 K, 331.2 and 441.6 GHz (upper traces), with simulations calculated with D/k_B = -6.4 K, E/k_B = -2.1 K (lower traces).

We emphasize here that the determination of the crystal field parameters based only upon magnetometry could be subject to a large degree of uncertainty, as several combinations of D, E, J can fit the $M(H)$ and $\chi T(T)$ data. However, the fitting of the very low temperature $C(T)$ yields a unique solution, which is confirmed by the HF-EPR analysis.

In other complexes, high-field high-frequency Electron Paramagnetic Resonance (EPR) or Inelastic Neutron Scattering (INS) have been used to determine accurately the single ion Mn(III) rhombicity. However, for the case of Mn(III)-Mn(III) dimers the determination of single-ion parameters is not straightforward as we have seen in this work, and has been discussed in ref. [58]

3.6 Dynamic Magnetic Properties

Ac susceptibility measurements in the frequency range $0.1 < f < 10^4$ Hz were performed as a function of temperature (1.8 – 4.3 K) and field strength (0 – 30 kOe). The average relaxation time at each temperature and field is determined from the maximum of the $\chi''(T,H)$ curves represented as a function of excitation frequency (Figures 12(a) and 12(b)), since at the maximum (χ''_{max}), $\tau = 1/2\pi f$.

At H = 0, for T < 4 K, a relaxation process at high frequency is detected, varying with temperature according to an Arrhenius law with an activation energy E_a/k_B = 5.6 ± 0.1 K, and τ_0 = 2.2 ± 0.1 10^{-6} s (Figure 12(d)). As the applied field is increased, the high frequency relaxation process time constant τ_{hf}, decreases, while a very slow relaxation process, inexistent at H = 0, sets on and increases in

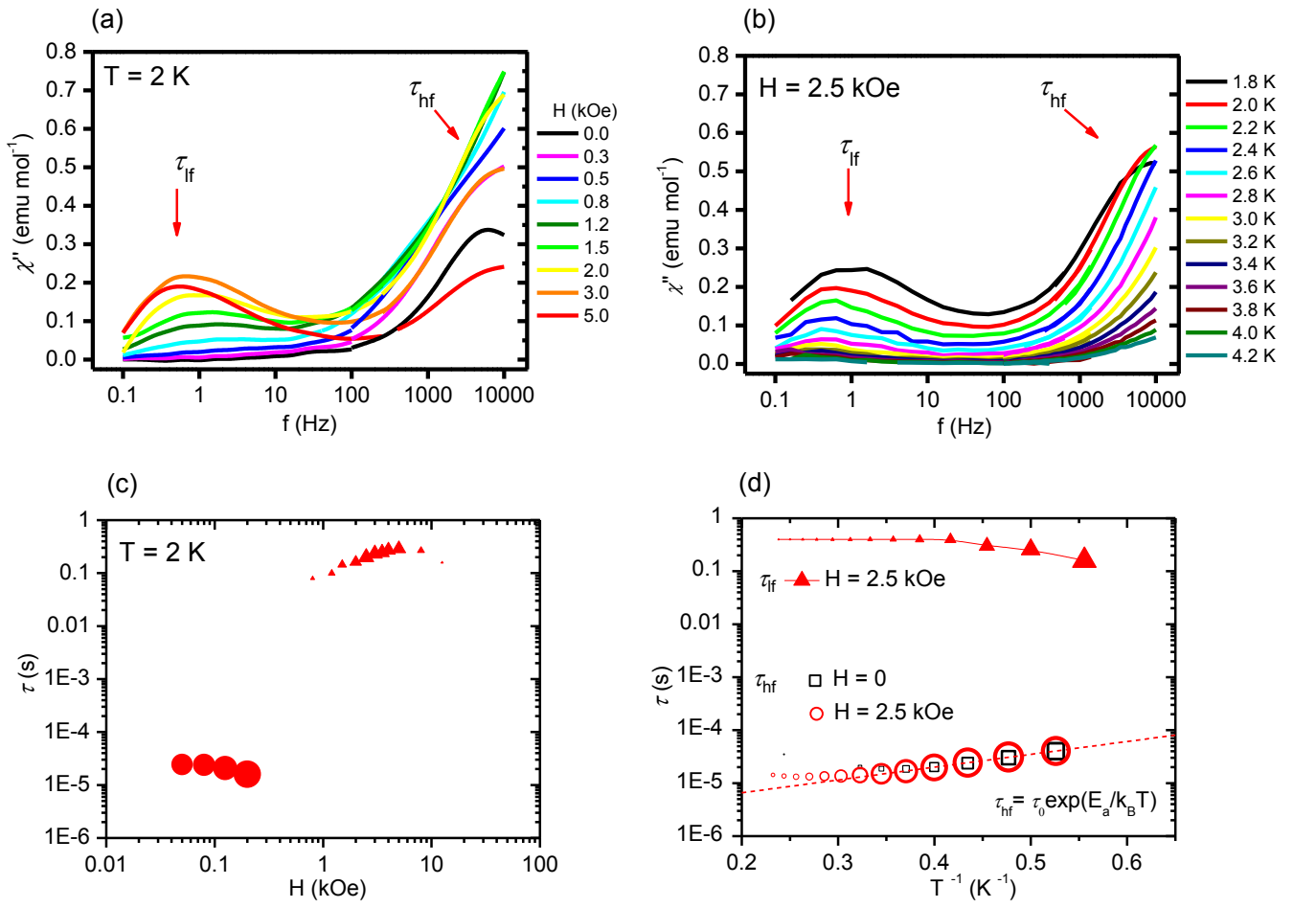

Figure 12. Out-of-phase component of the susceptibility as a function of the frequency, (a) at T = 2 K for various applied dc magnetic fields; (b) at H = 2.5 KOe at different temperatures; (c) relaxation time as a function of the magnetic field, at at T = 2 K; (d) relaxation times as a function of the inverse temperature; values for H = 0 kOe in black and for H = 2.5 kOe in red.

$\chi''_{max}(f)$ intensity till H = 3 kOe. Above that applied field $\chi''(f)$ decreases (Figure 12(a)). The field-dependence of the two observed relaxation times, τ_{lf} and τ_{hf}, is shown in Figure 12(c).

We associate the high frequency process to a spin-lattice Orbach process through the first excited cluster electronic state, since according to the model used to explain the static properties, the first electronic excited state lies at E_1/k_B = 15 K, which is compatible with the observed E_a.

The second, field-induced low frequency relaxation process is extremely slow, reaching τ_{lf} = 0.4 s at 5 kOe, and it decreases smoothly for decreasing temperature. This type of slow relaxation is systematically found in many magnetic compounds and may be associated to the field-induced onset of a direct spin-lattice relaxation process.[31,59,60,61,62,63] The presence of such a very slow process in all sort of magnetic complexes (transition metals, rare-earth metals or clusters), suggests that it is caused by a universal mechanism. One of the obvious candidates is magnetic relaxation slowing down by the phonon-bottleneck effect. This effect may take place in the transfer of energy from the spin system to the lattice, with a time constant τ_{sp}, and from the lattice to the thermal bath, with a time constant τ_{pb}.

The phonon bottleneck (PB) effect is relevant when, i) the heat generated by the excitation of the spin system by the ac field cannot be transferred because there are not sufficient phonons in the lattice vibration dispersion to absorb it, and/or ii) when the heat generated at the spin and lattice coupled modes cannot be evacuated to the bath because of weak thermal contact between the sample and the bath.

Magnetic relaxation in SMMs has been reported to be influenced by PB effects in some examples, where resonant trapping of low-energy phonons,[64,65] or poor thermal contact between the crystal and the bath,[66,67,68] have been proposed as the mechanisms responsible for the observed slow relaxation of the magnetization.

It has been shown[46,69] that the observed relaxation time τ_{obs} in presence of the PB effect can be correlated with τ_{sp} and τ_{pb} by the relation:

$$\tau_{obs} = \tau_{sp} + \frac{C_m + C_{lat}}{C_{lat}} \tau_{pb} = \tau_{sp} + b\,\tau_{pb} \ , \qquad [3]$$

where τ_{sp} is the spin relaxation time. At sufficiently high temperatures, where C_m is negligible in comparison to C_{lat}, and provided that there is a good thermal contact between the sample and the bath (isothermal limit), then $\tau_{obs} \approx \tau_{sp}$. However, as temperature decreases C_m may become larger than C_{lat}, and, as a consequence, $\tau_{obs} \approx b \cdot \tau_{pb}$. More importantly, poor thermal contact between sample and bath leads also to a phonon bottleneck situation, as τ_{pb} becomes very large. The ac magnetic field dynamically drives the spin system out of thermal equilibrium. An insufficient thermal contact of the sample with the heat bath slows down the relaxation of the spin system.

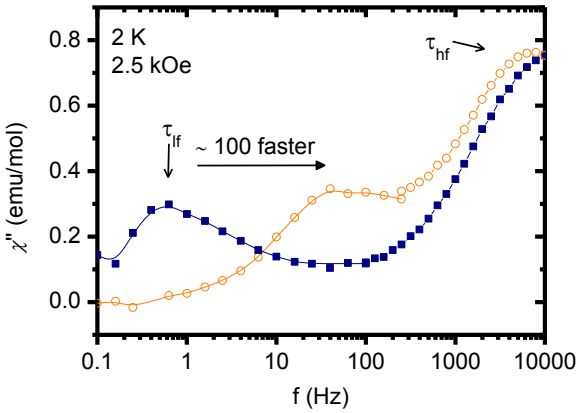

Figure 13. Out-of-phase component of the susceptibility at H = 2.5 kOe and T = 2 K as a function of frequency for different pressure conditions. Bold squares show standard pressure conditions (P < 0.1Torr) and open circles show results for atmospheric pressure.

The PB effect has been recently invoked to explain the $\tau \propto T^{-2}$ temperature dependence of a fast relaxation process in $[Mn_2O_2(bipy)_4](ClO_4)_3$,[31] and a Gd cyanoacetate polymer.[61] This dependence is predicted in presence of PB for direct processes, where just one phonon is emitted or absorbed during the relaxation process,[70] when the Resonant Phonon Trapping (RPT) takes place,[71] or when the magnetic heat capacity shows a $C_m \propto T^{-2}$ temperature dependence. However, if the relaxation process is of the Orbach type (i.e., two phonon processes take place by excitation and de-excitation to higher energy levels at E_a) the PB just renormalizes the characteristic relaxation time τ_0 to higher values, while the E_a remains the same.

We performed an ac susceptibility experiment as a function of the sample chamber He gas pressure to show how the thermal contact affects the spin relaxation time. In magnetic susceptibility measurements, the ac magnetic field is applied to the sample at low temperature, as the sample is immersed in a sample chamber with a low pressure of helium (P < 0.1 Torr at 2 K). The magnetic susceptibility at 2500 Oe and 2 K was measured for the sample chamber at atmospheric pressure of helium, enhancing thermal contact, and compared with standard measurement. As observed in Figure 13, improved thermal contact between sample and bath decreases the relaxation time (τ_{lf}) by about two orders of magnitude, while the high frequency relaxation time, associated to the Orbach process (τ_{hf}) is practically unchanged. A similar shift of the $\chi''(f)$ low frequency maximum to higher values has been shown to occur in KCr alum placed in a helium gas atmosphere when increasing its pressure[72].

In the present case, the existence of a fast relaxation of the Orbach type is proven already at H = 0, and the applied field hardly modifies the thermal activation energy. Therefore, the PB effect does not influence the fast relaxation time. This result is confirmed by the experiment presented in Figure 13, where the high frequency relaxation processes is practically not affected by the increased thermal contact of the sample with the bath. In contrast, the slow relaxation is only observable upon the application of an external field and has a $\tau \propto H^n$ dependence, with $n > 0$ for $H \leq$ 5kOe, and $n < 0$ at higher fields. This dependence seems to be caused by a direct process with its

relaxation time slowed down by the PB effect because of weak thermal contact between the sample and the bath and also, because at very low temperatures $C_m >> C_{lat}$.

The analysis of the effect of transverse anisotropy on magnetic relaxation deserves some attention. An important result of this work is the observation of magnetic relaxation for $T < 4$ K already at zero field. Some of the $Mn(III)_2$ dimeric complexes have shown slow magnetic relaxation at low temperatures, most of them upon application of an external field (see Table 1). However, in a few cases slow relaxation is also present at zero applied field. The $[Mn_2(saltmen)_2ReO_4)_2]$ is described as an out-of-plane dimer with each of the Mn(III) ions surrounded by N_2O_2 atoms of the $saltmen^{2-}$ ligand in the equatorial plane, and two axial oxygen atoms from the $[ReO_4]^-$ ion. The Jahn Teller distortion gives rise to an axial anisotropy of elongated form, with D/k_B = -4 K. The two Mn(III) are related crystallographically by an inversion center and the intradimer interaction is ferromagnetic, J/k_B = 2.65 K. This cluster has Single Molecule Magnet behavior at $H = 0$ and low temperatures.[20] In the dimeric cluster $[Mn(saltmen)(N_3)]_2$, we find O, N, N, O coordination in the equatorial plane, from the $saltmen^{2-}$ ligand and the apical atoms is N from the N_3^- and the oxygen from the phenolate group of $saltmen^{2-}$. The axial anisotropy decrease to D/k_B = -1.4 K and the intra-dimer interaction is also ferromagnetic with J/k_B = 0.86 K.[14]. The third reported case is the dimer $[Mn(5\text{-}Clsalpn)N_3]_2$ where the Jahn Teller elongation is along the N-Mn(III)-O, while in the equatorial plane one finds again a O, N. N. O coordination. The axial anisotropy is D/k_B = -1.44 K and J/k_B = 1 K, ferromagnetic once more.[23] In all cases, the intra-dimer interaction was found to be ferromagnetic. To describe the relaxation behavior only axial anisotropy was invoked.

In the present case, where slow relaxation is also observed at $H = 0$, the coordination, with equatorial 3 O, N, and long apical axis N-Mn-O, is different from all previously reported cases. It gives rise to rhombic distortion, as has been predicted by *ab initio* calculations and found by very low temperature heat capacity measurements and confirmed by HF-EPR experiments. Thus, the present sample provides an original case in the study of slow relaxation.

In most Mn(III) complexes, small deviations from axial symmetry, like transversal ligand field terms and hyperfine interaction, enhance quantum tunnelling of the magnetization (QTM) through the ground state. In the present compound, with an important rhombic distortion, E, slow relaxation of the magnetization is observed at zero field. This can be explained as due to the energy splitting of the ground state doublet, $\Delta_{2Mn} = 0.25$ K. This energy gap detunes quantum tunneling already at $H = 0$, allowing the observation of slow relaxation of the magnetization in our experimental frequency window. Despite the effect of the rhombic term in the zero field splitting is much lower for a dimeric Mn(III) compound compared to a monomeric one, the remarkably large rhombic distortion in this compound compensates this effect. The experimentally obtained energy barrier of the Orbach process, E_a/k_B = 5.6 K is of the same order as the energy of the first excited level, as obtained in the simulations, but a factor 2.7 lower. This evidences the mixing of excited states through the rhombic term and the effect of fourth order ZFS terms.

In conclusion, the above results evidence the huge effect of a large single-ion transverse anisotropy on the dynamic magnetic behaviour. The rhombic term E allows bistability in complexes which otherwise would relax through QTM and, additionally, it determines the anisotropy energy scale associated with the relaxation barrier.

Conclusions

The 2-(hydoxymethyl)pyridine is a good ligating unit for the preparation of a mixed manganese-calcium cluster complex based on a Mn_2Ca_2 core. In fact, **1** is the first Mn/Ca complex of any type to be obtained with hmp ligand. Magnetization measurements carried out on the complex as a function of field at different temperatures and magnetic temperature-dependent susceptibility measurements reflect a unique Mn(III) valence state over the whole temperature range, with a dimerization of the Mn ions at low temperatures. The Mn(III) ions in the cluster interact ferromagnetically with J/k_B = 1.1 K forming a dimer at low temperatures with a $S_T = 4$ ground state. The static magneto-thermal behaviour is explained with a single-ion orthorhombic ligand field, with ZFS parameters D/k_B = -6.4 K and a notably large E/k_B = -2.1 K, in good agreement with *ab initio* calculations. HF-EPR experiments confirm the single crystal parameters obtained from thermomagnetic measurements, clearly indicating an orthorhombic ratio E/D close to 1/3.

A significant result of this study is that the large E/D ratio of this compound, predicted by the *ab initio* calculations, was determined from the low temperature heat capacity measurements and confirmed by HF-EPR results. Since both experiments were performed on powder samples, the actual easy magnetization axis could not be determined. However, from the *ab initio* calculations we may conjecture that the EAM of Mn(III) in this complex is along the O1-Mn-N2 distorted octahedron long axis.

Ac magnetization measurements, in addition, reveals the slow relaxation characteristics of a SMM below 4 K. At $H = 0$ a magnetic relaxation process is observed at high frequencies ($\tau_{hf} \sim 10^{-5}$ s), identified as an Orbach-type mechanism with an energy barrier E_a/k_B = 5.6 K, associated to the large transversal single-ion distortion. Under an applied magnetic field, a second, very slow process ($\tau_{lf} \sim 0.2$ s) is induced, which is explained as a direct process strongly affected by phonon bottleneck effects. The large E/D rhombicity of each of the Mn(III) ions for the dimer enables the observation of slow relaxation of the magnetization at zero field, and determines the effective energy barrier.

Although all reported Mn(III) single-ion molecules show fast relaxation at zero applied field,[73] to our knowledge only a few dimeric complexes actually show slow relaxation at $H = 0$; i.e. SMM behavior: the Schiff base dimeric Mn(III) complexes $[Mn_2(saltmen)_2(ReO_4)_2]$ at very low temperature[20] and complex $[Mn(saltmen)(N_3)]_2$,[14] both with uniaxial single ion anisotropy. Thus, the present Mn_2Ca_2 dimeric compound is very peculiar, since the first and second coordination environment generates the large orthorhombicity that brings the dimer Mn(III)-Mn(III) entity to slow relaxation at zero field. In all other cases an applied field is necessary to induce SMM behavior.

Acknowledgements

This work has been financed by MECOM Projects MAT11/23791, MAT14/53921-R and CTQ2015-64486-R,

DGA IMANA Project E34, and Moldova State Program Project 14.518.02.05A.

References

1 C. S. Mullins and V. L. Pecoraro, *Coord. Chem. Rev.*, 2008, **252**, 416–443.

2 G. Aromí and E. K. Brechin, *Struct. Bond.*, 2006, **122**, 1–67.

3 M. Ferbinteanu, H. Miyasaka, W. Wernsdorfer, K. Nakata, K. I. Sugiura, M. Yamashita, C. Coulon and R. Clérac, *J. Am. Chem. Soc.*, 2005, **127**, 3090–3099.

4 J. Nugent, *Biochim. Biophys. Acta Bio-Energetics*, 2001, **1503**, 1.

5 J. Yano and V. Yachandra, *Chem. Rev.*, 2014, **114**, 4175–205.

6 J. P. McEvoy and G. W. Brudvig, *Chem. Rev.*, 2006, 106, 4455–4483.

7 S. Mukhopadhyay, S. K. Mandal, S. Bhaduri and W. H. Armstrong, *Chem. Rev.*, 2004, **104**, 3981–4026.

8 R. Sessoli, D. Gatteschi, A. Caneschi and M. A. Novak, *Nature*, 1993, **365**, 141–143.

9 D. Li, R. Clérac, S. Parkin, G. Wang, G. T. Yee and S. M. Holmes, *Inorg. Chem.*, 2006, **45**, 5251–5253.

10 A. M. Ako, I. J. Hewitt, V. Mereacre, R. Clérac, W. Wernsdorfer, C. E. Anson and A. K. Powell, *Angew. Chemie Int. Ed.*, 2006, **45**, 4926–4929.

11 R. Ishikawa, R. Miyamoto, H. Nojiri, B. K. Breedlove and M. Yamashita, *Inorg. Chem.*, 2013, **52**, 8300–8302.

12 A. J. Tasiopoulos, A. Vinslava, W. Wernsdorfer, K. Abboud and G. Christou, *Angew. Chemie - Int. Ed.*, 2004, **43**, 2117–2121.

13 C.-I. Yang, Z.-Z. Zhang and S.-B. Lin, *Coord. Chem. Rev.*, 2015, **289**–**290**, 289–314.

14 Z. Lu, M. Yuan, F. Pan, S. Gao, D. Zhang and D. Zhao, *Inorg. Chem.*, 2006, **45**, 3538–3548.

15 G. Bhargavi, M. V. Rajasekharan, J. P. Costes and J. P. Tuchagues, *Polyhedron*, 2009, **28**, 1253–1260.

16 Q. Wu, Y.-G. Li, Y.-H. Wang, R. Clérac, Y. Lu and E.-B. Wang, *Chem. Commun.*, 2009, **38**, 5743–5.

17 X. Liu and F. Wang, *Coord. Chem. Rev.*, 2012, **256**, 1115–1136.

18 A. J. Wu, J. E. Penner-Hahn and V. L. Pecoraro, *Chem. Rev.*, 2004, **104**, 903–938.

19 H. Miyasaka, A. Saitoh and S. Abe, *Coord. Chem. Rev.*, 2007, **251**, 2622–2664.

20 H. Miyasaka, R. Clérac, W. Wernsdorfer, L. Lecren, C. Bonhomme, K. I. Sugiura and M. Yamashita, *Angew. Chemie - Int. Ed.*, 2004, **43**, 2801–2805.

21 G. Rajaraman, E. C. Sañudo, M. Helliwell, S. Piligkos, W. Wernsdorfer, G. Christou and E. K. Brechin, *Polyhedron*, 2005, **24**, 2450–2454.

22 Y. Sawada, W. Kosaka, Y. Hayashi and H. Miyasaka, *Inorg. Chem.*, 2012, **51**, 4824–32.

23 G. Bhargavi, M. V Rajasekharan, J.-P. Costes and J.-P. Tuchagues, *Dalton Trans.*, 2013, **42**, 8113–23.

24 T.-T. Wang, M. Ren, S.-S. Bao and L.-M. Zheng, *Eur. J. Inorg. Chem.*, 2014, **6**, 1042–1050.

25 I. J. Hewitt, J.-K. Tang, N. T. Madhu, R. Clerac, G. Buth, C. E. Anson and A. K. Powell, *Chem. Commun.*, 2006, **9**, 2650–2652.

26 H. Fliegl, K. Fink, W. Klopper, C. E. Anson, A. K. Powell and R. Clérac, *Phys. Chem. Chem. Phys.*, 2009, **11**, 3900–9.

27 N. Li, M. Wang, C.-B. Ma, M.-Q. Hu, R.-W. Zhou, H. Chen and C.-N. Chen, *Inorg. Chem. Commun.*, 2010, **13**, 730–732.

28 E. S. Koumousi, S. Mukherjee, C. M. Beavers, S. J. Teat, G. Christou and T. C. Stamatatos, *Chem. Commun.*, 2011, **47**, 11128–30.

29 V. Kotzabasaki, M. Siczek, T. Lis and C. J. Milios, *Inorg. Chem. Commun.*, 2011, **14**, 213–216.

30 V. Krewald, F. Neese and D. A. Pantazis, *J. Am. Chem. Soc.*, 2013, **135**, 5726–39.

31 A. C. Benniston, S. Melnic, C. Turta, A. B. Arauzo, J. Bartolomé, E. Bartolomé, R. W. Harrington and M. R. Probert, *Dalt. Trans.*, 2014, **43**, 13349–13357.

32 T. Taguchi, T. C. Stamatatos, K. A. Abboud, C. M. Jones, K. M. Poole, T. A. O'Brien and G. Christou, *Inorg. Chem.*, 2008, **47**, 4095–4108.

33 P. L. Feng, C. C. Beedle, C. Koo, W. Wernsdorfer, M. Nakano, S. Hill and D. N. Hendrickson, *Inorg. Chem.*, 2008, **47**, 3188–3204.

34 J. Feuersenger, D. Prodius, V. Mereacre, R. Clérac, C. E. Anson and A. K. Powell, *Inorg. Chem. Commun.*, 2011, **14**, 1851–1854.

35 F. He, M. L. Tong and X. M. Chen, *Inorg. Chem.*, 2005, **44**, 8285–8292.

36 A. L. Barra, L. C. Brunel and J. B. Robert, *Chem. Phys. Lett.*, 1990, **165**, 107–109.

37 *CrysAlis RED, Oxford Diffr. Ltd., Version 1.171.36.32*, 2003.

38 O. V. Dolomanov, L. J. Bourhis, R. J. Gildea, J. A. K. Howard and H. Puschmann, *J. Appl. Crystallogr.*, 2009, **42**, 339–341.

39 G. M. Sheldrick, *Acta Crystallogr. A.*, 2008, **64**, 112–22.

40 T. Sala and M. V. Sargent, *J. Chem. Soc. Chem. Commun.*, 1978, 253.

41 J. B. Vincent, H. R. Chang, K. Folting, J. C. Huffman, G. Christou and D. N. Hendrickson, *J. Am. Chem. Soc.*, 1987, **109**, 5703–5711.

42 L. B. Jerzykiewicz, J. Utko, M. Duczmal, P. Starynowicz and P. Sobota, *Eur. J. Inorg. Chem.*, 2010, **28**, 4492–4498.

43 C. Angeli, R. Cimiraglia, S. Evangelisti, T. Leininger and J.-P. Malrieu, *J. Chem. Phys.*, 2001, **114**, 10252.

44 F. Neese, *ORCA Progr. Syst. WIREs Comput Mol Sci.*, 2012, **2**, 73–78.

45 D. A. Pantazis, X.-Y. Chen, C. R. Landis and F. Neese, *J. Chem. Theory Comput.*, 2008, **4**, 908–19.

46 A. Abragam and B. Bleaney, in *Electron Paramagnetic Resonance of Transition Ions*, Clarendon Press - Oxford, 1970, p. Chapter 10.

47 H. Nagao, M. Nishino, Y. Shigeta, T. Soda, Y. Kitagawa, T.

Onishi, Y. Yoshioka and K. Yamaguchi, *Coord. Chem. Rev.*, 2000, **198**, 265–295.

48 A. D. Becke, *J. Chem. Phys.*, 1993, **98**, 5648.

49 J. J. Borrás-Almenar, J. M. Clemente Juan, E. Coronado and B. S. Tsukerblat, *J. Comput. Chem.*, 2001, **22**, 985–991.

50 J. Krzystek, G. J. Yeagle, J.-H. Park, R. D. Britt, M. W. Meisel, L.-C. Brunel and J. Telser, *Inorg. Chem.*, 2003, **42**, 4610–4618.

51 T. Goto, T. Kubo, T. Koshiba, Y. Fujii, A. Oyamada, J. Arai, K. Takeda and K. Awaga, *Phys. B*, 2000, **284**–**288**, 1227–1228.

52 C. Duboc, D. Ganyushin, K. Sivalingam, M. N. Collomb and F. Neese, *J. Phys. Chem. A*, 2010, **114**, 10750–10758.

53 K. S. Pedersen, M. Sigrist, H. Weihe, P. L. W. Tregenna-Piggott, M. Schau-Magnussen, J. Dreiser, H. Mutka, A.-L. Barra and J. Bendix, *Inorg. Chem. Commun.*, 2012, **24**, 24–28.

54 A. Grigoropoulos, M. Pissas, P. Papatolis, V. Psycharis, P. Kyritsis and Y. Sanakis, *Inorg. Chem.*, 2013, **52**, 12869–12871.

55 I. Ciofini and C. A. Daul, *Coord. Chem. Rev.*, 2003, **238**, 187–209.

56 J. P. Malrieu, R. Caballol, C. J. Calzado, C. de Graaf and N. Guihéry, *Chem. Rev.*, 2014, **114**, 429–492.

57 S. Stoll and A. Schweiger, *J. Magn. Reson.*, 2006, **178**, 42–55.

58 M. Retegan, M.-N. Collomb, F. Neese and C. Duboc, *Phys. Chem. Chem. Phys.*, 2013, **15**, 223–234.

59 E. Bartolomé, J. Bartolomé, S. Melnic, D. Prodius, S. Shova, A. Arauzo, J. Luzón, F. Luis and C. Turta, *Dalt. Trans.*, 2013, **42**, 10153–10171.

60 E. Bartolomé, J. Bartolomé, S. Melnic, D. Prodius, S. Shova, A. Arauzo, J. Luzón, L. Badía-Romano, F. Luis and C. Turta, *Dalton Trans.*, 2014, **43**, 10999–1013.

61 A. Arauzo, A. Lazarescu, S. Shova, E. Bartolomé, R. Cases, J. Luzón, J. Bartolomé and C. Turta, *Dalton Trans.*, 2014, **43**, 12342–12356.

62 E. Bartolomé, J. Bartolomé, A. Arauzo, J. Luzón, L. Badía, R. Cases, F. Luis, S. Melnic, D. Prodius, S. Shova and C. Turta, *J. Mater. Chem. C*, 2016, **4**, 5038–5050.

63 P. Car, M. Perfetti, M. Mannini, A. Favre, A. Caneschi and R. Sessoli, *Chem. Commun.*, 2011, **47**, 3751–3753.

64 M. Orendáč, L. Sedláková, E. Čižmár, A. Orendáčová, A. Feher, S. A. Zvyagin, J. Wosnitza, W. H. Zhu, Z. M. Wang and S. Gao, *Phys. Rev. B - Condens. Matter Mater. Phys.*, 2010, **81**, 1–8.

65 A. Rossin, G. Giambastiani, M. Peruzzini and R. Sessoli, *Inorg. Chem.*, 2012, **51**, 6962–6968.

66 I. Chiorescu, W. Wernsdorfer, A. Müller, H. Bögge and B. Barbara, *Phys. Rev. Lett.*, 2000, **84**, 3454–3457.

67 R. Schenker, M. N. Leuenberger, G. Chaboussant, D. Loss and H. U. Güdel, *Phys. Rev. B - Condens. Matter Mater. Phys.*, 2005, **72**.

68 K. Petukhov, S. Bahr, W. Wernsdorfer, A. L. Barra and V. Mosser, *Phys. Rev. B - Condens. Matter Mater. Phys.*, 2007, **75**, 1–12.

69 J. Flokstra, G. J. Gerritsma, G. A. Hartemink and L. C. Van Der Marel, *Physica*, 1974, **77**, 99–120.

70 P. L. Scott and C. D. Jeffries, *Phys. Rev.*, 1962, **127**, 32.

71 D. L. Huber, *Phys. Rev.*, 1965, **139**, 1684–1686.

72 G. J. Gerritsma, J. Flokstra, G. A. Hartemink, J. J. M. Scholten, A. J. W. A. Vermeulen and L. C. van der Marel, *Phys. B+C*, 1978, **95**, 173–182.

73 G. A. Craig, J. J. Marbey, S. Hill, O. Roubeau, S. Parsons and M. Murrie, *Inorg. Chem.*, 2015, **54**, 13–5.